Manuscript
Click here to access/download;Manuscript;Revised_Manuscript.docx

SHEAR STRENGTH MODEL FOR RC BEAMS WITH U-WRAPPED FRCM COMPOSITES

Tommaso D'Antino[a*], Francesco Focacci[b], Lesley H. Sneed[c], Carlo Pellegrino[d]

[a]Politecnico di Milano, Piazza Leonardo da Vinci, 20133 Milan, Italy

[b]Università eCampus, Via Isimbardi 10, 22060 Novedrate, Italy

[c]Missouri University of Science and Technology, 1401 North Pine Street, Rolla, MO, 65409, USA

[d]University of Padova, via Marzolo 9, 35131 Padova, Italy

Abstract

The shear strength of reinforced concrete (RC) elements can be improved by applying externally bonded (EB) fiber-reinforced cementitious matrix (FRCM) composites. FRCM composites are generally U-wrapped around the cross-section of RC beams and completely wrapped around the cross-section of RC columns. When the U-wrapped layout is employed, composite debonding usually occurs before the tensile strength of the composite can be attained. However, depending on the specific FRCM adopted, different failure modes can be observed. Although the use of FRCM composites to strengthen existing RC members is gaining popularity, limited work has been done to formulate a reliable design procedure for FRCM shear strengthening of RC members. In this paper, a model is proposed to compute the shear strength contribution of FRCM composite U-wrapped around RC members. The model, which is an extension of the model used for fiber-reinforced polymer (FRP) shear strengthened beams, is based on mechanical considerations, does not contain empirical coefficients, and can be applied to any FRCM composite provided that its bond behavior and tensile strength are identified. The model is validated by comparing the analytical predictions with the experimental results of RC beams strengthened in shear

* Corresponding author: tommaso.dantino@polimi.it

with PBO and carbon FRCM composites found in the literature. Finally, an example of the evaluation of the shear capacity associated with the FRCM reinforcement is provided to illustrate the use of the model.

Introduction

Inorganic-matrix composites represent a promising alternative to organic-matrix composites for strengthening existing reinforced concrete (RC) and masonry structures. Within the broad category of inorganic-matrix composite materials, fiber-reinforced cementitious matrix (FRCM) composites have been gaining popularity in recent years as externally-bonded (EB) strengthening of RC structural elements. FRCM composites are typically comprised of high-strength open-mesh fiber textiles embedded within a cementitious matrix that is responsible for the stress-transfer between the fibers and the substrate. FRCM composites might be preferred to well-known fiber-reinforced polymer (FRP) composites in certain applications because they have good chemical and physical compatibility with the substrate and allow its transpiration, do not suffer from exposure to sunlight, and do not produce toxic smoke in the case of fire (ACI 549.4R 2013).

Experimental research has proven that FRCM composites may be used as EB reinforcement to enhance the bending (Täljsten et al. 2007, Hashemi and Al-Mahaidi 2012, Babaeidarabad et al. 2014, Sneed et al. 2016), shear (Tetta et al. 2015, Ombres 2015, Escrig et al. 2015, Loreto et al. 2015, Tzoura and Triantafillou 2016, Gonzalez-Libreros et al. 2017), and torsional (Alabdulhady and Sneed 2018) strength of RC beams and columns and to improve the behavior of RC elements mainly subjected to axial loads (Di Ludovico et al. 2010, Thermou et al. 2015, Sneed et al. 2017). Although FRCM composites have been employed to strengthen real concrete and masonry structures (D'Ambrisi et al. 2015), limited work has been carried out to provide design procedures for these materials. Different authors have proposed analytical models to compute the flexural strength of RC beams (Bencardino et al. 2018), masonry walls (D'Antino et al. 2018), and masonry arches (Alecci et al. 2016, Alecci et al. 2017) strengthened with EB

FRCM. Currently the only available design guideline is the American ACI 549.4R (2013), in which the provisions are based on mechanical characterization of the FRCM composite by means of tensile tests using the clevis-grip method (AC434 2013).

For the case of EB FRP composites, the shear strength of strengthened RC elements, V_u, is generally computed by adding the contribution provided by the composite material, V_f, to the shear strength of the unstrengthened element, V_{un} (ACI 440.2R 2017, CNR-DT 200 2004, CNR-DT 200 R1 2013) as shown in Eq. (1):

$$V_u = V_{un} + V_f \tag{1}$$

V_f is generally computed according to the Mörsch truss (Khalifa et al. 1998):

$$V_f = 2n\sigma_{fe}t_f d_{fe}\frac{w_f}{i_f}\left(\cot\theta + \cot\beta\right)\sin\beta \tag{2}$$

where n is the number of layers of composite reinforcement applied on each side of the beam, t_f is the equivalent thickness of each layer of fibers, d_{fe} is the composite shear reinforcement effective depth as defined by the specific guideline considered, w_f is the width of each composite strip, i_f is the center-to-center spacing between the composite strips measured orthogonally to the beam longitudinal axis, θ and β are the inclination angles of the compressed strut and of the fibers with respect to the beam longitudinal axis, and σ_{fe} is the design tensile strength (i.e. the effective stress) of the composite shear reinforcement. Eq. (2) assumes that failure occurs due to a main diagonal crack, whose inclination coincides with the inclination θ of the compressed strut , and that the composite on both sides of the beam provides the same contribution to the shear strength.

According to Eq. (1), the shear strength V_u is attained when V_{un} and V_f simultaneously reach their respective maximum values. However, experimental observations and analytical works have shown that the presence of EB shear reinforcement may affect the contribution of the internal steel reinforcement, sometimes leading to a limited increase of V_u with respect to V_{un} (Pellegrino and Modena 2002, Ali et al.

2006, Grande et al. 2009, Chen et al. 2013, Gonzalez-Libreros et al. 2017). This aspect is not discussed in this paper, where Eq. (1) is assumed to be valid (TR 55 2012, CNR-DT 200 R1 2013, ACI 440.2R 2017).

The effective stress σ_{fe} is the average tensile stress in the composite bridging a shear crack and depends mainly on the layout of the EB reinforcement and on the shear stress transfer mechanism at the FRP-concrete interface (Triantafillou 1998, Sas et al. 2009, Foraboschi 2012). In particular, according to CNR-DT 200 R1 (2013), σ_{fe} is computed on the basis of the bond capacity, defined as the maximum force transferable at the reinforcement-substrate interface, and the effective bond length l_{eff} of the reinforcement, defined as the minimum bonded length needed to attain the bond capacity.

ACI 549.4R (2013) follows a similar approach for FRCM composites, but the effective stress σ_{fe} is computed by multiplying the design tensile strain - obtained by clevis-grip tensile tests and enforcing an upper bound limit of 0.004 - by the tensile modulus of elasticity of the cracked FRCM composite measured in the second stage of the clevis-grip test (ACI 549.4R 2013, AC434 2013, D'Antino et al. 2018). Employing the elastic modulus provided by ACI 549.4R (2013), Ombres (2015) applied the design approach proposed by the Italian CNR-DT 200 (2004) for FRP shear strengthening to compute the effective stress σ_{fe} and the shear strength contribution V_f of FRCM strengthened beams. Similarly, the design model proposed by Chen and Teng (2003) for FRP shear strengthening was recalibrated by Tetta et al. (2018) to best fit the experimental data in a database comprising FRCM shear strengthened beams. It should be noted that both the CNR-DT 200 (2004) and Chen and Teng (2003) models consider that the composite tensile stress varies along the shear crack depending also on the composite bonded length.

The effective stress σ_{fe} depends on the bond properties of the composite material. Since the FRCM-concrete bond properties can be quantitatively and qualitatively different from the FRP-concrete bond

properties, the formulations used for the evaluation of σ_{fe} for FRP composites may not be applicable for FRCM composites. Therefore, formulations that take into account the bond behavior of the specific FRCM composite adopted are needed to use the design approach based on the effective stress σ_{fe} of EB FRCM.

In this paper, an analytical model to compute the shear strength contribution of an EB FRCM composite to an RC element, V_f, is provided. The model is an extension of that commonly employed for FRP shear strengthened beams (TR 55 2012, CNR-DT 200 R1 2013, ACI 440.2R 2017) and is applied to the U-wrapped layout. The model, which is based on mechanical considerations and does not contain empirical coefficients, accounts for the bond behavior and failure mode of the specific FRCM considered. Therefore, it can be applied to any FRCM composite provided that its bond behavior, i.e. its bond capacity and effective bond length, is clearly identified. Because the shear strength contribution of an EB composite is related to the bond between the composite and substrate, especially for U-wrapped configurations (Gonzalez-Libreros et al. 2017), this paper discusses the FRCM bond behavior and the relationship between the peak load and bonded length, which form the basis for the model presented. The proposed model is validated with test results reported in the literature, and an example of the evaluation of the shear capacity associated with the FRCM reinforcement is provided (see the Appendix).

Background on the evaluation of the effective stress σ_{fe} for the U-wrap configuration

According to Eq. (2), the contribution of the EB composite V_f to the shear strength of RC beams depends on the inclination θ of the compressed strut, the composite layout, and the effective stress σ_{fe}. The force F_f in the composite material (Fig. 1) is computed considering a main diagonal crack with the crack tip located at the centroid of the flexural compression zone, which is commonly accepted for truss models. Indeed, this assumption is necessary to model the member as a truss structure and is useful to simplify

115 the evaluation of the effective stress. Only the composite crossing the main diagonal crack is assumed to
116 contribute to the beam shear capacity.
117 Fig. 1a shows the tensile stress in some fibers of the EB composite. These fibers have different bonded
118 lengths and are associated with different crack openings of the main diagonal crack, which entails for
119 different fiber tensile stresses. This is because the stress $\sigma(\xi)$ of the fiber at the abscissa ξ depends on the
120 interfacial slip *s* at the loaded end of the composite (i.e. at the shear crack) and on the available bonded
121 length $\ell=\ell(\xi)$. Thus, the stress $\sigma(\xi)=\sigma(s,\ell)$, where *s* and ℓ are functions of ξ, can be evaluated
122 based on the load response of a bond test with bonded length ℓ (Fig. 1). In general (CNR-DT 200 R1
123 2013), the crack opening $w(\xi)$ is assumed to be linear (Fig. 2). Therefore $w(\xi)=\alpha\xi$, where α is the crack
124 opening angle. This particular crack shape was found to provide conservative results in the case of EB
125 FRP shear strengthening (Chen and Teng 2003, Chen et al. 2013). Non-linear crack shapes, which
126 account for the actual stress field in the beam, may be adopted but would lead to a more complex
127 formulation of σ_{fe}.
128 When debonding of the composite material governs the shear strength, the force F_f is (Monti and Liotta
129 2007):

130 $$F_f = 2\cdot n\cdot t_f \max_{\alpha}\int_{\xi_0}^{\xi_1}\sigma(s,\ell)\,d\xi \tag{3}$$

131 where

132 $$\ell(\xi)=\xi\frac{\sin\theta}{\sin\beta} \tag{4}$$

133 is the bonded length of the fiber along the crack at the abscissa ξ, and $\Delta\xi_{cr}=\xi_1-\xi_0$ is the length of the main
134 diagonal crack crossed by the fibers (Fig. 2.)
135 Under the assumption of a linear crack, in Eq. (3) the slip *s* of the fiber at the abscissa ξ depends on the
136 crack opening angle α (Fig. 2):

$$s = s(\alpha,\xi) = \frac{1}{2}\alpha \cdot \xi \cdot \sin(\theta + \beta) \tag{5}$$

The evaluation of F_f by means of Eq. (3) requires the knowledge of the load responses $\sigma(s)$ (Fig. 1b) associated with the bonded lengths ℓ in the range $\xi_0 \sin\theta/\sin\beta = \ell(\xi_0) \le \ell \le \ell(\xi_1) = \xi_1 \sin\theta/\sin\beta$, or alternatively, the knowledge of the cohesive material law (CML) of the composite material employed, since it allows the analytical computation of $\sigma(s)$ for different ℓ (Focacci et al. 2017). According to Monti and Liotta (2007), the maximum value of the integral in Eq. (3) with respect to α corresponds to the simultaneous attainment of the peak stresses $\sigma^*(\ell)$ of the load responses associated with the bonded lengths ℓ in the range $\ell(\xi_0) \le \ell \le \ell(\xi_1)$. In this case, the evaluation of F_f requires only the knowledge of the relationship between the peak stress σ^* and the bonded length ℓ, $\sigma^*(\ell)$, named the σ^*- ℓ curve or capacity response (Fig. 1c) in this paper:

$$F_f = 2 \cdot n \cdot t_f \int_{\xi_0}^{\xi_1} \sigma^*(\ell(\xi))\, d\xi \tag{6}$$

This result may not be strictly applicable for all FRCM composites, which may show load and capacity responses different from those observed for FRP composites. Furthermore, assuming that failure occurs when the composite fibers attain their peak stress simultaneously may not accurately describe the debonding process, which is a dynamic phenomenon often triggered by the debonding of a small portion of the composite strip. However, the assumption that the maximum value of the integral in Eq. (3) is equal to the integral in Eq. (6) allows for a simple solution of the problem and is commonly employed for shear strength models of FRP strengthened beams. Therefore, it is adopted in this paper as a first attempt to provide a simple formulation that can be used for design purposes. According to Chen and Teng (2003), Monti and Liotta (2007), and CNR-DT 200 R1 (2013), σ_{fe} is the average stress in the composite bridging the shear crack at shear failure:

158 $$\sigma_{fe} = \frac{F_f}{2(\xi_1 - \xi_0)} = \frac{n \cdot t_f}{\xi_1 - \xi_0} \int_{\xi_0}^{\xi_1} \sigma^*(\ell(\xi))\, d\xi \quad (7)$$

159 Therefore, the estimation of σ_{fe} requires the knowledge of the capacity response of the specific composite
160 employed.

161 Experimental results indicated that the load response and capacity response depend on the number of
162 fiber layers *n*. Increasing *n* does not lead to a linearly proportional increase of the stresses in the load and
163 capacity responses because the number of layers affects the mechanical properties of the material and
164 may lead to different failure modes (D'Ambrisi et al. 2012). Therefore, $\sigma(s)$ and $\sigma^*(\ell)$ curves should
165 be obtained experimentally for each number of layers considered in order to apply Eqs. (3), (6), and (7).
166 Although extensive work has been done to investigate the bond behavior of FRP composites applied to
167 different substrates (see e.g. Chen and Teng 2001, Dai et al. 2006, Carloni and Subramaniam 2010, 2012,
168 Carrara and Ferretti 2013), the results obtained could not be applied to the case of FRCM composites
169 due to important differences in their bond behaviors (Bencardino et al. 2018). For this reason, analytical
170 models formulated for FRP shear strengthening of RC members should be applied accounting for the
171 different bond behavior observed for FRCM composites.

172 According to the Mörsch truss, only the longitudinal fibers in the composite, i.e. the fibers wrapped
173 around the cross-section, provide a contribution to F_f. If bidirectional fiber sheets are employed, the
174 transversal fibers could contrast the opening of the shear crack, especially if the composite is continuous
175 along the member length. The contribution of the transversal fibers is usually neglected (CNR-DT 200
176 R1 2013, ACI 440.2R 2017).

177 As noted in the "Introduction" section, Eq. (1) is based on the simultaneous attainment of V_{un} and V_f.
178 Although this assumption needs further verification, it appears reasonable in the case of FRCM
179 composites that are characterized by high values of the debonding slip s_f (Thermou et al. 2015, D'Ambrisi

et al. 2012, D'Ambrisi et al. 2015, Carabba et al. 2017), which in turn entails for a crack opening sufficient to yield the transversal steel reinforcement.

FRCM bond behavior

Since failure of FRCM strengthened elements generally occurs due to composite debonding, numerous studies have been carried out to investigate the bond behavior of different FRCM composites using direct-shear test set-ups. The experimental observations showed that debonding of FRCM composites may occur at different interfaces, namely A) at the matrix-fiber interface with slippage of the fibers (D'Antino et al. 2014), B) at the matrix-fiber interface with damage of the matrix (Carabba et al. 2017), C) at the matrix-substrate interface without damage of the substrate (Babaeidarabad et al. 2014), and D) at the matrix-substrate interface with detachment of a thin layer of the substrate (Raoof et al. 2016). When a single layer of fibers is employed, debonding generally occurs due to failure mode (A), which can also be followed by tensile rupture of the fibers (Napoli and Realfonzo 2015). Results of single-lap direct-shear tests of polyparaphenylene benzobisoxazole (PBO) FRCM-concrete joints were employed in (D'Antino et al. 2014) to identify an idealized load response for FRCM-concrete joints and to identify the interface CML, i.e. the interfacial shear stress-slip relationship $\tau(s)$. According to the fracture mechanics approach adopted in (D'Antino et al. 2014), the load response for any bonded length and the capacity response (Fig. 1) can be obtained by the solution of the differential equation given in Eq. (8) that governs the bond problem (Focacci et al. 2017):

$$\frac{d^2 s}{dy^2} = \frac{p_f}{E_f A_f} \tau(s) \tag{8}$$

where y is the coordinate along the bonded length, p_f is the contact perimeter of the debonding interface, E_f is the elastic modulus of the fibers, and $A_f = w_f \cdot t_f$ is the cross-sectional area of the fibers. Procedures on

202 how to identify the FRCM-substrate CML can be found in (D'Ambrisi et al. 2012, D'Antino et al. 2014,
203 Focacci et al. 2017).
204 Eq. (8) can be used for any FRCM composite provided that the CML and p_f are clearly identified
205 (D'Antino et al. 2018). Fig. 3a and Fig. 3b show the debonding interfaces and corresponding contact
206 perimeter of a portion of composite-substrate joints with infinitesimal length dy in the case of matrix-
207 fiber debonding (failure mode A) and cohesive debonding within the substrate (failure mode D),
208 respectively. In the former case, since n=1 for one layer of fiber, the contact perimeter p_f can be assumed
209 equal to two times the width of the fiber strip w_f with the fibers considered as evenly distributed. In the
210 case of cohesive debonding within the substrate, the contact perimeter is equal to w_f.
211 For some FRCM composites, debonding of the fibers within the embedding matrix resulted in
212 friction/interlocking at the matrix-fiber interface. The presence of friction is responsible for a residual
213 constant interfacial shear stress τ_f for slip s higher than a certain slip s_f (Fig. 3c). Within a fracture
214 mechanics framework, the debonding stress σ_{deb}, which is the stress at the onset of debonding, can be
215 obtained as (Focacci et al. 2017):

216
$$\sigma_{deb} = \sqrt{2E_f G_F \frac{p_f}{A_f}} \tag{9}$$

217 where

218
$$G_F = \int_0^{s_f} \tau(s)ds \tag{10}$$

219 It should be noted that, if $\tau(s)$ is a cohesive material law, G_F should not include any contribution of
220 friction. However, if a macro-fracture model is adopted to obtain the $\tau(s)$ relation from experimental
221 tests, the contribution of friction cannot be separated from the bond contribution (D'Antino et al. 2014).
222 Therefore:

$$G_F = G_F^c + G_f \tag{11}$$

where G_F^c and G_f are the energy contributions provided by bond and friction only, respectively. In this paper, the friction shear stress is assumed to increase linearly from s=0 to s=s_f and is equal to τ_f for $s \geq s_f$ (see hatched region in Fig. 3c). This assumption represents a first and simple attempt to account for the contribution of friction during the debonding process, which could not be measured experimentally. Under this assumption, the work per unit surface done by the friction shear stress from s=0 to s=s_f is:

$$G_f = \frac{s_f \cdot \tau_f}{2} \tag{12}$$

and the stress σ_b provided by bond only at the onset of debonding is:

$$\sigma_b = \sqrt{\frac{2E_f p_f}{A_f}\left(G_F - G_f\right)} = \sqrt{\sigma_{deb}^2 - \frac{E_f p_f s_f \tau_f}{A_f}} \tag{13}$$

The presence of friction affects the FRCM-concrete joint load and capacity responses, which were introduced in Fig. 1. To illustrate the bond behavior of a composite with and without friction, two different CMLs, named (i) and (ii), respectively, are depicted in Fig. 3c, and the corresponding idealized load responses are shown in Fig. 3d. CMLs (i) and (ii) are assumed to have the same slip at the onset of debonding s_f, although the resulting effective bond length and load carrying capacity are different.

Fig. 3d shows the load responses associated with CML (i) in the case of bonded length ℓ longer and less than the composite effective bond length $l_{eff,i}$, where i indicates that it is associated with CML (i). The idealized load response associated with CML (ii) and bonded length longer than the corresponding effective bond length $l_{eff,ii}$, associated with CML (ii), is also provided in Fig. 3d.

According to the idealized load responses (Fig. 3d), if the bonded length is equal to or longer than the effective bond length, increasing the loaded end slip leads to an increase of the applied load, and the load carrying capacity σ_{deb} can be attained. For the composite with friction (CML (i) in Fig. 3c) and $\ell > l_{eff,i}$, further increase of the loaded end slip results in a linear increase of the applied stress up to the peak stress

σ^*. After the peak stress σ^* is attained, the applied stress decreases until reaching a constant value σ_f due to friction only. The presence of the snap-back phenomenon shown in Fig. 3d for the bonded lengths longer than the effective bond length is due to the elastic energy release of the unbonded fibers consequent to the decrease of the applied load. Further discussion on this phenomenon can be found in Carrara and Ferretti (2013) and Barbieri et al. (2016) for the case of FRP-concrete joints and in D'Antino et al. (2018) for the case of FRCM-concrete joints.

For the composite without friction, i.e. τ_f=0 (see CML (ii) in Fig. 3c), and $\ell > l_{eff,ii}$, the load remains constant and equal to σ_{deb} after the onset of debonding (i.e. $\sigma^*=\sigma_{deb}$), and no residual stress is observed at the completion of the test (i.e. σ_f=0). In both cases, with and without friction, if the bonded length is less than the effective bond length, the load carrying capacity cannot be reached, and failure occurs with $\sigma^*<\sigma_{deb}$. For the composite with friction and $\ell < l_{eff,i}$, a residual stress is observed at the end of the test, whereas for the composite without friction, σ_f=0 at the end of the test.

Fig. 3e shows the capacity responses constructed from CMLs (i) and (ii) within the fracture mechanics framework adopted in (D'Antino et al. 2014). From Fig. 3e it is clear that the presence of friction is responsible for an increase of the peak stress σ^* for bonded lengths longer than $l_{eff,i}$, whereas a constant peak stress $\sigma^*=\sigma_{deb}$ is observed when $\ell > l_{eff,ii}$ and τ_f =0. The friction stress τ_f can be computed from the residual stress σ_f as $\tau_f = \sigma_f \cdot A_f/(p_f \cdot \ell)$. Therefore, the slope of the σ^*-ℓ curve when $\tau_f \neq 0$ is equal to m:

$$m = \frac{p_f \tau_f}{A_f} \tag{14}$$

Assuming various shapes of the CML, which were obtained by an inverse calibration method applied to the results of direct-shear tests of PBO FRCM-concrete joints, different σ^*-ℓ curves were presented by Focacci et al. (2017). The adoption of different CML functions allowed for investigating the effect of their shapes on the results obtained. Selected CMLs and the resulting σ^*-ℓ curves are plotted in Fig. 4a

and Fig. 4b, respectively, whereas the key parameters of the corresponding CMLs are reported in Table 1. The effective bond length of the PBO FRCM composite considered was estimated to be l_{eff}=260 mm, with a corresponding debonding stress σ_{deb}=1908 MPa. The mechanical characteristics of the PBO FRCM constituents are listed in Table 2. Further details on how the CMLs were calibrated and employed to solve the bond problem differential equation can be found in (Focacci et al. 2017).

Peak stress σ^*– bonded length ℓ analytical solutions

As discussed in the "Background on the evaluation of the effective stress σ_{fe} for the U-wrap configuration" section, the evaluation of σ_{fe} needs the knowledge of the capacity response. If the CML and p_f are identified (Focacci et al. 2017), the $\sigma^*(\ell)$ function can be constructed solving the differential equation given in Eq. (8). However, it should be noted that Eq. (8) may fail to capture the behavior for short bonded lengths, which showed different failure modes than those observed for long bonded lengths (D'Antino et al. 2014). Alternatively, an approximated $\sigma^*(\ell)$ function can be employed.

In this paper, two new functions are proposed to obtain a well-approximated capacity response without knowing the CML and solving Eq. (8). Advantages and limitations of each function are presented within this section. The parameters controlling the shape of the proposed functions can be adjusted to represent the bond behavior of different FRP and FRCM composites.

The first function represents an exponential trend of the peak stress:

$$\sigma^*(\ell) = \sigma_e^*(\ell) = \left(\sigma_{deb} - m \cdot l_{eff}\right) \frac{1 - e^{-b \cdot \ell}}{1 - e^{-b \cdot l_{eff}}} + m \cdot \ell \tag{15}$$

where b is a parameter that controls the shape of the σ^*-ℓ curve for low values of the bonded length.

The second function represents a cubic-linear trend of the peak stress:

$$\sigma^*(\ell)=\sigma_3^*(\ell)=\begin{cases} c\cdot\ell+\dfrac{\ell^3\left(c\cdot l_{eff}-2\sigma_{deb}+m\cdot l_{eff}\right)}{l_{eff}^3}-\dfrac{\ell^2\left(2c\cdot l_{eff}-3\sigma_{deb}+m\cdot l_{eff}\right)}{l_{eff}^2} & \text{for} \quad \ell\le l_{eff} \\ m\left(\ell-l_{eff}\right)+\sigma_{deb} & \text{for} \quad \ell> l_{eff} \end{cases} \tag{16}$$

where c is a parameter that controls the shape of the σ^*-ℓ curve for $\ell\le l_{eff}$.

Both functions given in Eqs. (15) and (16) pass through the point (σ_{deb}, l_{eff}), and their derivatives at that point are continuous. Furthermore, they are based on the assumption that the friction shear stress τ_f remains constant for any slip s larger than s_f, which entails for a linear increase of the σ^*-ℓ curve for bonded lengths longer than l_{eff}.

Eq. (15) can be employed only in the case of $\tau_f\neq 0$, whereas Eq. (16) can be employed for any value of τ_f. If $\tau_f=0$, and consequently $m=0$, Eq. (16) becomes a piecewise function that represents a parabolic-rectangular trend of the peak stress:

$$\sigma^*(\ell)=\sigma_2^*(\ell)=\begin{cases} \sigma_{deb}\dfrac{\ell}{l_{eff}}\left(2-\dfrac{\ell}{l_{eff}}\right) & \text{for} \quad \ell\le l_{eff} \\ \sigma_{deb} & \text{for} \quad \ell> l_{eff} \end{cases} \tag{17}$$

Eq. (17) has also been used to describe the σ^*-ℓ curve for FRP (Monti and Liotta 2007) and is the basis of the EB FRP shear design model of the Italian CNR-DT 200 R1 (2013).

In Eqs. (15)-(17) subscripts "*e*", "3", and "2" are used to indicate that the peak stress is computed assuming an exponential (Eq. (15)), cubic-linear (Eq (16)), and parabolic-rectangular (Eq. (17)) shape of the σ^*-ℓ relationship, respectively.

The function given in Eq. (15) is particularly convenient when bond test results for different bonded lengths are available because it can be used to fit the experimental outcomes without distinguishing between $\ell\le l_{eff}$ and $\ell> l_{eff}$. Eq. (16) is convenient when the values of σ_{deb} and τ_f are known. If results from bond tests with different bonded lengths are available, both the parameters b and c can be obtained by best fitting the experimental results with the proposed functions. Alternatively, these parameters can be

determined as a function of the friction shear stress τ_f, the debonding stress σ_{deb}, and the effective bond length l_{eff}.

The ratio between the integrals from ℓ=0 to ℓ=l_{eff} of Eqs. (15) and (16) and the integral for the same limits of integration of Eq. (17) is due to the presence of friction:

$$\int_0^{l_{eff}} \sigma_e^*(\ell)\,\mathrm{d}\ell = \eta \cdot \int_0^{l_{eff}} \sigma_2^*(\ell)\,\mathrm{d}\ell \tag{18}$$

$$\int_0^{l_{eff}} \sigma_3^*(\ell)\,\mathrm{d}\ell = \eta \cdot \int_0^{l_{eff}} \sigma_2^*(\ell)\,\mathrm{d}\ell \tag{19}$$

where η is a multiplier related to friction. In this paper, η is estimated as the ratio between the debonding stress σ_{deb} and the bond stress σ_b:

$$\eta = \frac{\sigma_{deb}}{\sigma_b} \tag{20}$$

Substituting Eqs. (9) and (13) into Eq. (20), η can be obtained as:

$$\eta = \sigma_{deb}\sqrt{\frac{A_f}{\sigma_{deb}^2 A_f - E_f p_f s_f \tau_f}} \tag{21}$$

Substituting Eq. (21) into Eq. (18) provides Eq. (22), which can be solved numerically to obtain parameter *b*:

$$\frac{3}{2bl_{eff}}\left(\sigma_{deb} - m\cdot l_{eff}\right)\frac{b\cdot l_{eff} + e^{-b\cdot l_{eff}} - 1}{1 - e^{-b\cdot l_{eff}}} + \frac{3m\cdot l_{eff}}{4} = \sqrt{\frac{\sigma_{deb}^4 A_f}{\sigma_{deb}^2 A_f - E_f p_f s_f \tau_f}} \tag{22}$$

Substituting Eq. (21) into Eq. (19), the parameter *c* can be obtained:

$$c = m - \frac{\sigma_{deb}}{l_{eff}}\left(6 - 8\sigma_{deb}\sqrt{\frac{A_f}{\sigma_{deb}^2 A_f - E_f p_f s_f \tau_f}}\right) \tag{23}$$

The σ^*-ℓ curves determined by Eqs. (15) and (16) with $\tau_f \neq 0$, and by Eq. (17) with τ_f=0, where *b* and *c* were obtained by Eqs. (22) and (23) for the case of PBO FRCM-concrete joints reported in (D'Antino et

al. 2014, Carloni et al. 2015), respectively, are depicted in Fig. 4b and compared with the experimental results and the analytical capacity responses associated with the CMLs calibrated in (Focacci et al. 2017). Both functions given in Eqs. (15) and (16) describe the experimental σ^*-ℓ behavior and reproduce the analytical responses obtained by solving the differential equation in Eq. (8) with good accuracy. It should be noted that the results shown in Fig. 4b were obtained by bond tests with the slip and applied load parallel to the fiber direction. In FRCM shear strengthened beams, the direction of the fibers is generally not perpendicular to the crack axis, which entails for a slip with components perpendicular and parallel to the longitudinal fiber. This effect is not accounted for in this work due to the lack of the experimental investigations on the effect of fiber-load misalignment.

Finally, the maximum value of the peak stress provided by Eqs. (15) and (16) should be limited to the tensile strength of the fibers σ_f, which defines the terminal point on the σ^*-ℓ curve. The bonded length needed to attain σ_f, named the maximum bond length l_{max}, is provided by Eqs. (24) and (25) for the exponential and cubic-linear functions, respectively:

$$l_{max,e} = \sigma_f - \left(\sigma_{deb} - m \cdot l_{eff}\right) \frac{\left(1 - e^{-b \cdot l_{max,e}}\right)}{m\left(1 - e^{-b \cdot l_{eff}}\right)} \tag{24}$$

$$l_{max,3} = l_{eff} + \frac{\sigma_f - \sigma_{deb}}{m} \tag{25}$$

Since Eq. (24) does not allow a closed-form solution, Eq. (25) could be employed to obtain a reasonable approximation of the maximum bond length associated to Eq. (15). In the case of Eq. (17), a maximum bonded length is not defined since the absence of friction does not allow for an increase of the fiber tensile stress after the onset of debonding.

Analytical model for U-wrapped configuration

Shear failure is assumed to occur due to a single main diagonal shear crack, and the shear strength is obtained according to the Mörsch truss (TR 55 2012, CNR-DT 200 R1 2013, ACI 440.2R 2017) with the contribution of the EB reinforcement computed as discussed in the "Background on the evaluation of the effective stress σ_{fe} for the U-wrap configuration" section. The shear strength provided by the FRCM composite is then computed by Eq. (2), where the effective stress σ_{fe} is evaluated with Eq. (7) with $\sigma^*(\ell)$ given by Eq. (15) or (16) when the bond phenomenon includes friction and given by Eq. (17) when it does not. Therefore, the proposed model applies when debonding of the composite governs the shear strength. However, for FRCM composites with $\tau_f \neq 0$, the model also takes into account the possible tensile failure of the fibers after the onset of debonding.

As shown in Fig. 5, only the EB reinforcement located between the crack tip and the centroid of the internal flexural tension reinforcement is considered. This simplification leads to conservative results because the contribution of the composite above the crack tip and below the flexural tension reinforcement is neglected.

When the FRCM composite is U-wrapped around the member web, the available bonded length varies with the coordinate ξ along the crack axis according to Eq. (4). According to the previous assumptions, Eq. (4) is valid for ξ in the range $0 \le \xi \le z/\sin\theta$ if the EB reinforcement is extended at least up to the centroid of the compressive force (as shown in Fig. 5) and in the range $\left(z - d_f\right)/\sin\theta \le \xi \le d_f/\sin\theta$ if the EB reinforcement is not extended up to the flexural compression zone of the beam, where z is the inner lever arm, i.e. the distance between the centroids of the flexural compression zone and flexural tension reinforcement, and d_f (Fig. 5).

Assuming that the fibers of the tensile composite truss simultaneously attain the peak of the load response associated with their respective available bonded lengths, Eqs. (15) and (16) can be employed for the computation of σ_{fe}. Eq. (7) with the $\sigma^*(\ell)$ function given by Eq. (15) provides the effective stress:

$$\sigma_{fe,e} = \frac{m \cdot L_{max}}{2} - \frac{\left(\sigma_{deb} - m l_{eff}\right)\left(e^{-b \cdot L_{max}} + b \cdot L_{max} - 1\right)}{b \cdot L_{max}\left(e^{-b \cdot l_{eff}} - 1\right)} \le \sigma_{e,max} \tag{26}$$

where

$$\sigma_{e,max} = \frac{m \cdot l_{max,e}}{2} - \frac{\left(\sigma_{deb} - m l_{eff}\right)\left(e^{-b \cdot l_{max,e}} + b \cdot l_{max,e} - 1\right)}{b \cdot l_{max,e}\left(e^{-b \cdot l_{eff}} - 1\right)} \tag{27}$$

is the effective stress associated with the attainment of the tensile strength of the fibers according to Eq. (15).

If Eq. (16) is employed for the $\sigma^*(\ell)$ relation, Eq. (7) provides the effective stress:

$$\sigma_{fe,3} = \begin{cases} L_{max}\left[\left(\frac{L_{max}}{2}\right)^2 \frac{l_{eff}\left(c+m\right) - 2\sigma_{deb}}{l_{eff}^3} + \frac{L_{max}}{3}\frac{3\sigma_{deb} - l_{eff}\left(2c+m\right)}{l_{eff}^2} + \frac{c}{2}\right] \text{ for } L_{max} < l_{eff} < l_{max,3} \\ \frac{1}{L_{max}}\left\{\left[\sigma_{deb} + \frac{m}{2}\left(L_{max} - l_{eff}\right)\right]\left(L_{max} - l_{eff}\right) + l_{eff}\frac{6\sigma_{deb} + l_{eff}\left(c-m\right)}{12}\right\} \text{ for } l_{eff} < L_{max} < l_{max,3} \end{cases} \le \sigma_{3,max} \tag{28}$$

where

$$\sigma_{3,max} = \frac{m}{m l_{eff} + \sigma_f - \sigma_{deb}}\left[\frac{\sigma_f^2 - \sigma_{deb}^2}{2m} + l_{eff}\frac{6\sigma_{deb} + l_{eff}\left(c-m\right)}{12}\right] \tag{29}$$

is the effective stress associated with the attainment of the tensile strength of the fibers according to Eq. (16).

In Eqs. (26) and (28) $L_{max} = \min\{z, d_f\}/\sin(\beta)$ is the maximum available bonded length (Fig. 5).

If τ_f=0, Eq. (16) becomes the parabolic-rectangular function of Eq. (17), and the FRCM effective stress is:

$$\sigma_{fe,2} = \begin{cases} \sigma_{deb} \dfrac{L_{max}}{l_{eff}} \left(1 - \dfrac{1}{3} \dfrac{L_{max}}{l_{eff}} \right) & \text{for } L_{max} \le l_{eff} \\ \sigma_{deb} \left(1 - \dfrac{1}{3} \dfrac{l_{eff}}{L_{max}} \right) & \text{for } L_{max} > l_{eff} \end{cases} \quad (30)$$

Since Eq. (30) implicitly assumes that the debonding stress is lower than the fiber tensile strength and the absence of friction does not allow for an increase of the fiber tensile stress after the onset of debonding, fiber tensile failure could not occur. In Eqs. (26)-(30), the crack is assumed to have a length $\Delta\xi_{cr}=\xi_1-\xi_0=\min\{z,d_f\}/\sin(\theta)$ (Fig. 5).

Validation of the model

In this section, the accuracy of the model is assessed by comparing experimental and analytical results of RC beams strengthened in shear with FRCM composites in terms of V_f. Since the model requires the knowledge of the FRCM bond behavior, i.e. the capacity response or the cohesive material law, it could be validated considering only those beams strengthened with FRCM composites for which $\sigma^*(\ell)$ or $\tau(s)$ was provided. Therefore, all available beams strengthened with U-wrapped PBO FRCM composite and some beams strengthened with carbon FRCM composite were considered for the model validation. Although additional experimental tests on FRCM strengthened RC beams are available in the literature, they could not be considered because the bond behavior of the specific composite employed was not available.

Four beams strengthened with U-wrapped PBO FRCM composite (Ombres 2015, Escrig et al. 2015) and two beams strengthened with U-wrapped carbon FRCM composite (Gonzalez-Libreros et al. 2017) were collected from the literature. All beams had a rectangular cross-section, included longitudinal and

transversal internal steel reinforcement, and were strengthened with one layer of either discrete FRCM strips (1 beam) or a continuous FRCM sheet (5 beams) that extended up to the compression edge, which provides $d=d_f$. The PBO fibers were in the form of an unbalanced open-mesh textile, with a weight of 70.2 g/m^2 and 17.8 g/m^2 in the longitudinal and transversal directions of the textile, respectively. The debonding stress, effective bond length, and friction shear stress of the PBO FRCM composite are σ_{deb}=1908 MPa, l_{eff}=260 mm, τ_f=0.03 MPa, respectively (see the "Peak stress σ^*– bonded length ℓ analytical solutions" section). The balanced carbon textile, with an overall area weight of 170.0 g/m^2, had σ_{deb}=1080 MPa and τ_f=0.01 MPa (Carozzi et al. 2017). The effective bond length of the carbon textile was assumed equal to l_{eff}=300 mm based on the results of a round robin test campaign carried out by the Rilem Technical Committee 250-CSM (Composites for the sustainable strengthening of masonry) (De Santis et al. 2017). All beams failed due to debonding of the composite at the matrix-fiber interface. The beam and composite characteristics, including the geometry, material properties, and experimental results, are summarized in Table 3.

Table 3 reports the shear strength contribution provided by the FRCM composite obtained experimentally, $V_{f,exp}$, computed as the difference between the shear strength of the strengthened beam and that of the corresponding unstrengthened beam in accordance with Eq. (1). In addition, the angle θ of the main shear crack with respect to the beam longitudinal axis, which was reported or measured using photographs or sketches provided in the corresponding reference, is provided in Table 3.

Values of the FRCM effective stress obtained by the exponential ($\sigma_{fe,e}$) and cubic-linear ($\sigma_{fe,3}$) shapes of the σ^*-ℓ curve and assuming z=0.9d are reported in Table 4 for the beams considered. Values of the parameters b, c, and m were determined with Eqs. (22), (23), and (14), respectively. For comparison, the contribution of friction was neglected by setting τ_f equal to 0, and the resulting effective stress $\sigma_{fe,2}$ is included in Table 4. The results show that close values were obtained for $\sigma_{fe,e}$ and $\sigma_{fe,3}$ (difference less

427 than 0.45% and 7.05% for PBO and carbon fibers, respectively), which confirms that the functions in
428 Eqs. (15) and (16) provide approximately the same results. Values of $\sigma_{fe,2}$ are approximately 10% lower
429 than the corresponding values of $\sigma_{fe,3}$ and $\sigma_{fe,e}$ for both PBO and carbon fibers, which indicates that the
430 contribution of friction to the effective stress is relatively small for the composites considered.
431 The crack length considered $\Delta\xi_{cr}$ and the crack length at which σ_{deb} is attained $\Delta\xi_a=\xi_{eff}-\xi_0$ (see Fig. 5) are
432 also reported in Table 4. For all beams, $\Delta\xi_{cr}<\Delta\xi_a$, which indicates that the composite could not attain its
433 load carrying capacity σ_{deb} at any fiber along the shear crack. This circumstance is not common for FRP
434 composites, for which the effective bond length is on the order of 100-200 mm, but could be common
435 for FRCM composites, which have been reported to have effective bond lengths between 150 mm and
436 300 mm (D'Antino et al. 2014, Askouni and Papanicolaou 2017, Santandrea et al. 2017). Table 4 also
437 reports the crack length needed to attain the fiber tensile strength σ_f (see Table 3) denoted
438 $\xi_{max}=l_{max,3}\cdot\sin(\beta)/\sin(\theta)$, where $l_{max,3}$ was computed by Eq. (25). The values of ξ_{max} obtained show that it
439 would be difficult to obtain tensile failure of the fibers for the PBO FRCM composite considered unless
440 the beam cross-section is particularly deep and/or the angle β is small.
441 Using the values of the effective stress obtained, Eq. (2) was employed to compute the FRCM
442 contribution to the shear strength V_f, setting $d_{fe}=\min\{0.9d,d_f\}$. The results obtained with the different
443 functions, reported in Table 4, show that the model provides a reasonably accurate estimation of the
444 experimental composite shear strength. To measure the model accuracy, percentage ratios $r_{x,y}$ between
445 the experimental and analytical values were computed for the different functions and are included in
446 Table 4:

447
$$r_{x,y}=\frac{V_{f,x}}{V_{f,y}}-1 \quad x,y=exp,e,3,2 \tag{31}$$

448 Positive values of $r_{exp,y}$ indicate that the analytical model underestimates the experimental result, whereas
449 negative values indicate an overestimation of $V_{f,exp}$. The results obtained show that the model
450 overestimates the experimental shear strength contribution for four beams, while slightly underestimated
451 results were obtained for the remaining two beams. As noted previously, results for the cubic-linear and
452 exponential functions are quite similar. The best accuracy was obtained with the exponential function in
453 the case of beam TRB1 ($r_{exp,e}$=1.1%), whereas the largest difference was observed with the same function
454 for beam TRA2 ($r_{exp,e}$=-30.7%). The discrepancy observed between some experimental and analytical
455 results could be attributed to different parameters, e.g. the scatter of the experimental results and the
456 assumption of simultaneous attainment of the maximum values of all shear resisting contributions in the
457 beam. Furthermore, the angle θ adopted is an average inclination of the main shear crack, while its
458 direction usually varies along its path. It should be noted that assuming θ=45°, as usually adopted for
459 design of composite shear strengthening (TR 55 2012, ACI 440.2R 2017, ACI 549.4R 2013), will provide
460 more conservative results than those obtained with the values of θ reported for the beams considered.
461 Values of $r_{3,2}$ and $r_{e,2}$ indicate that the contribution of friction ranges between 1.9-10.2% of the analytical
462 shear strength.
463 The authors are currently working to assess the accuracy of the model with respect to RC beams
464 strengthened with different FRCM composites. In particular, further work is needed to validate the model
465 accuracy when the bonded length is sufficient to fully develop the FRCM load carrying capacity and the
466 presence of friction results in an increase of the fiber tensile stress after the onset of debonding. This
467 process will allow also to verify if a limit on the fiber strain, analogous to that provided by ACI 549.4R
468 (2013) as noted in the "Introduction" section, should be enforced.
469

Conclusions

An analytical model to compute the shear strength of RC members U-wrapped with FRCM composites was presented in this paper. The model, which is an extension of the model used for FRP shear strengthened beams, is based on the Mörsch truss and accounts for the non-uniform composite tensile stress distribution along the shear crack. Two functions were put forward to describe the relation between the peak stress provided by FRCM bond tests and the associated bonded length, namely an exponential function and a piecewise cubic-linear function. Both proposed functions take into account the (possible) presence of a friction stress observed in FRCM bond tests. The two functions were used to describe the composite tensile stress distribution along the shear crack and to compute the composite effective stress. The exponential function can be adopted only for FRCM composites that show a friction contribution and is convenient when results of bond tests with different bonded length are available. The cubic-linear function can be applied to FRCM composites with or without the presence of friction, and its use is convenient when the debonding stress and friction shear stress are known. Furthermore, for the case without friction, the cubic-linear function reduces to the equation used in the model of the Italian CNR-DT 200 R1 (2013) for EB FRP composites. The comparison between the proposed model and the experimental results of beams strengthened in shear with PBO and carbon FRCM composites showed good accuracy of the model. Further comparison with a broad range of FRCM strengthened RC beams will provide further indications on the accuracy of the model.

Appendix - Example of design of RC beam shear strengthened with an EB U-wrapped carbon FRCM

This example shows the calculation of the shear strength contribution of a 1-layer carbon FRCM composite U-wrapped around an RC beam cross-section. The beam has a T-shaped cross-section and contains internal longitudinal reinforcement in the flexural tension zone and transverse shear

reinforcement (stirrups). The carbon FRCM is U-wrapped continuously along the entire length of the beam and extends up to the height of the web with the longitudinal fibers oriented orthogonal to the beam longitudinal axis. The carbon FRCM composite is comprised of a balanced open-mesh textile with a center-to-center spacing of 10 mm, embedded within a cementitious matrix. Bond tests showed that failure of carbon FRCM-concrete joints occurs due to debonding at the matrix-fiber interface, with the presence of interfacial friction. The shear strength provided by the EB carbon FRCM is computed as follows:

RC beam properties

Cross-section flange width B=500 mm.

Cross-section web width b_w=250 mm.

Cross-section height h=500 mm.

Cross-section web height h_w=400 mm.

Distance between the extreme compression surface and the centroid of the flexural tension reinforcement d=470 mm.

Flexural tension reinforcement area (4 bars with diameter ϕ=16 mm) A_s=804 mm^2.

Transverse reinforcement area (closed stirrups with diameter ϕ=8 mm, spaced at 250 mm) A_w=100 mm^2.

FRCM properties

Textile weight per unit area including both longitudinal and transversal directions of fiber sheet γ=220 g/m^2.

Equivalent fiber thickness per direction t_f=0.060 mm.

Fiber tensile strength σ_f=1800 MPa.

Fiber elastic modulus E_f=220 GPa.

Debonding stress σ_{deb}=1100 MPa.

Effective bond length l_{eff}=250 mm.

Friction stress (considering the fiber as evenly distributed) τ_f=0.025 MPa.

Slip at the onset of debonding s_f=1.20 mm.

Angle of the longitudinal fibers with respect to the beam longitudinal axis β=90°.

Shear strength of the U-wrapped carbon FRCM

The cubic-linear function provided in Eq. (16) is adopted. Since the FRCM composite showed the presence of friction, the first step is the determination of the parameters *m* (Eq. (14)) and *c* (Eq. (23)), obtained considering a continuous FRCM strip of width w_f=1000 mm with evenly distributed fibers:

$$p_f = 2w_f = 2000 \text{ mm} \tag{32}$$

$$A_f = t_f \cdot w_f = 60 \text{ mm}^2 \tag{33}$$

$$m = \frac{p_f \tau_f}{A_f} = 0.833 \frac{\text{N}}{\text{mm}^3} \tag{34}$$

$$c = m - \frac{\sigma_{deb}}{l_{eff}} \left(6 - 8\sigma_{deb} \sqrt{\frac{A_f}{\sigma_{deb}^2 A_f - E_f p_f s_f \tau_f}} \right) = 13.35 \frac{\text{N}}{\text{mm}^3} \tag{35}$$

The maximum bonded length l_{max} is obtained by Eq. (25):

$$l_{max} = l_{eff} + \frac{\sigma_f - \sigma_{deb}}{m} = 1090 \text{ mm} \tag{36}$$

Since the maximum available bonded length, namely L_{max}=min{z=0.9*d*,d_f=h_w}/sin(β)=400 mm, is longer than the effective bond length but less than l_{max}, debonding of the composite will occur before FRCM rupture, and Eq. (28) for l_{eff}<L_{max}<$l_{max,3}$ is employed to compute the composite effective stress:

$$\sigma_{fe} = \frac{1}{L_{max}} \left\{ \left[\sigma_{deb} + \frac{m}{2} \left(L_{max} - l_{eff} \right) \right] \left(L_{max} - l_{eff} \right) + l_{eff} \frac{6\sigma_{deb} + l_{eff} \left(c - m \right)}{12} \right\} = 943 \text{ MPa} \tag{37}$$

Assuming (conservatively) a crack inclination angle equal to θ=45°, the contribution of the carbon FRCM to the RC beam shear strength is:

$$V_f = 2n\sigma_{fe}t_f d_{fe}\frac{w_f}{i_f}\left(\cot\theta+\cot\beta\right)\sin\beta=45.25\ \text{kN} \quad (38)$$

where $d_{fe}=\min\{0.9d,d_f\}=400$ mm, and $w_f/i_f=1$ since the composite is continuous along the beam length.

Data Availability Statement

All data, models, and code generated or used during the study appear in the submitted article.

References

ACI (American Concrete Institute). (2013). "Guide to Design and construction of externally bonded fabric-reinforced cementitious matrix (FRCM) systems for repair and strengthening concrete and masonry structures." *ACI 549.4R-13*, Farmington Hills, MI.

ACI (American Concrete Institute). (2017). "Guide for the design and construction of externally bonded FRP systems for strengthening concrete structures." *ACI 440.2R-17*, Farmington Hills, MI.

Alabdulhady, M., and Sneed, L. H. (2018). "A Study of the Effect of Fiber Orientation on the Torsional Behavior of RC Beams Strengthened with PBO-FRCM Composite." Constr. Build. Mater., 166, 839-54.

Alecci, V., Focacci, F., Rovero, L., Stipo, G., and De Stefano, M. (2016). "Extrados strengthening of brick masonry arches with PBO-FRCM composites: experimental and analytical investigations." Compos. Struct., 149, 184-96.

Alecci, V., Focacci, F., Rovero, L., Stipo, G., and De Stefano, M. (2017). "Intrados strengthening of brick masonry arches with different FRCM composites: experimental and analytical investigations." Compos. Struct., 176, 898-909.

Ali, M. S. M., Oehlers, D. J., and Seracino, R. (2006). "Vertical shear interaction model between external FRP transverse plates and internal steel stirrups." Eng. Struct., 28(3), 381-389.

559 Askouni, P. D., and Papanicolaou, C. G. (2017). “Experimental investigation of bond between glass
560 textile reinforced mortar overlays and masonry: the effect of bond length.” Mater. Struct., 50(164), 1–
561 15.
562 Babaeidarabad, S., Loreto, G., and Nanni, A. (2014). “Flexural strengthening of RC beams with an
563 externally bonded fabric-reinforced cementitious matrix.” J. Compos. Constr.,
564 10.1061/(ASCE)CC.1943-5614.0000473, 04014009.
565 Barbieri, G., Biolzi, L., Bocciarelli, M., Cattaneo, S. (2016) “Size and shape effect in the pull-out of
566 FRP reinforcement from concrete.” Comp. Struct., 143, 395-417.
567 Bazant, Z. P., and Planas, J. (1997). *Fracture and size effect in concrete and other quasi-brittle*
568 *materials*, CRC Press, Boca Raton, Florida.
569 Bencardino, F., Carloni, C., Condello, A., Focacci, F., Napoli, A., and Realfonzo R. (2018). “Flexural
570 behavior of RC members strengthened with FRCM: State-of-the-art and predictive formulas.” Comp.
571 Part B, 148, 132-148.
572 Carabba, L., Santandrea, M., Carloni, C., Manzi, S., Bignozzi, M. C. (2017). “Steel fiber reinforced
573 geopolymer matrix (S-FRGM) composites applied to reinforced concrete structures for strengthening
574 applications: A preliminary study.” Compos. Part B, 128, 83-90.
575 Carloni, C., and Subramaniam, K. V. (2010). “Direct determination of cohesive stress transfer during
576 debonding of FRP from concrete.” Comp. Struct., 93(1), 184-192.
577 Carloni, C., and Subramaniam, K. V. (2012). “FRP/masonry debonding: numerical and experimental
578 study of mortar joints.” J. Compos. Constr., 10.1061/(ASCE)CC.1943-5614.0000282, 581-589.
579 Carloni, C., D’Antino, T., Sneed, L. H., Pellegrino, C. (2015). “Role of the matrix layers in the stress-
580 transfer mechanism of FRCM composites bonded to a concrete substrate.” J. Eng. Mech., 141(6),
581 10.1061/(ASCE)EM.1943-7889.0000883, 04014165.

582 Carozzi, F.G., Bellini, A., D'Antino, T., de Felice, G., Focacci, F., Hojdys, L., Laghi, L., Lanoye, E.,
583 Micelli, F., Panizza, M., Poggi, C. (2017), "Experimental investigation of tensile and bond properties of
584 carbon-FRCM composites for strengthening masonry elements", Compos. Part B, 128, 100-119.
585 Carrara, P., and Ferretti, D. (2013). "A finite-difference model with mixed interface laws for shear tests
586 of FRP plates bonded to concrete." Compos. Part B, 54, 329-342.
587 Chen, G. M., Teng, J. G., and Chen, J. F. (2013). "Shear strength model for FRP-strengthened RC beams
588 with adverse FRP-steel interaction." J. Compos. Constr., 10.1061/(ASCE)CC.1943-5614.0000313, 50-
589 66.
590 Chen, J. F., and Teng, J. G. (2001). "Anchorage strength models for FRP and steel plates bonded to
591 concrete." J. Struct. Eng., 127(7), 784-791.
592 Chen, J. F., and Teng, J. G. (2003). "Shear capacity of FRP-strengthened RC beams: FRP debonding."
593 Constr. Build. Mater., 17(1), 27–41.
594 D'Ambrisi, A., Feo, L., and Focacci, F. (2012). "Bond-slip relations for PBO-FRCM materials
595 externally bonded to concrete." Compos. Part B, 43(8), 2938–2949.
596 D'Ambrisi, A., Focacci, F., Luciano, R., Alecci, V., and De Stefano, M. (2015). "Carbon-FRCM
597 materials for structural upgrade of masonry arch road bridges." Comp. Part B, 75, 355-66.
598 D'Antino, T., Carloni, C., Sneed, L. H., and Pellegrino, C. (2014). "Matrix-fiber bond behavior in PBO
599 FRCM composites: A fracture mechanics approach." Eng. Fract. Mech., 117, 94-11.
600 D'Antino, T., Colombi, P., Carloni, C., Sneed, L.H. (2018). "Estimation of a matrix-fiber interface
601 cohesive material law in FRCM concrete joints." Compos. Struct., 193, 103-112.
602 D'Antino, T., Carozzi, F. G., Colombi, P., and Poggi, C. (2018). "Out-of-plane maximum resisting
603 bending moment of masonry walls strengthened with FRCM composites." Comp. Struct., 202, 881-96.
604 Dai, J. G., Ueda, T., and Sato, Y. (2006). "Unified analytical approaches for determining shear bond
605 characteristics of FRP-concrete interfaces through pullout tests." J. Adv. Concr. Tech., 4, 133-145.

606 De Santis, S., Carozzi, F. G., de Felice, G., Poggi, C. (2017). "Test methods for Textile Reinforced
607 Mortar Systems." Compos. Part B, 127, 121-132.
608 Di Ludovico, M., Prota, A., and Manfredi, G. (2010). "Structural upgrade using basalt fibers for
609 concrete confinement." J. Compos. Constr., 14(5), 541–52.
610 Escrig, C., Gil, L., Bernat-Maso, E., and Puigvert, F. (2015). "Experimental and analytical study of
611 reinforced concrete beams shear strengthened with different types of textile-reinforced mortar." Constr.
612 Build. Mater., 83, 248–60.
613 Focacci, F., D'Antino, T., Carloni, C., Sneed, L. H., and Pellegrino, C. (2017). "An indirect method to
614 calibrate the interfacial cohesive material law for FRCM-concrete joints." Mater. Design, 128, 206-217.
615 Foraboschi, P. (2012). "Shear strength computation of reinforced concrete beams strengthened with
616 composite materials." Compos.: Mech., Comput., App., 3(3), 227-252.
617 Gonzalez-Libreros, J. H., Pellegrino, C., D'Antino, T., and Sneed, L. H. (2017). "Evaluation of external
618 transversal reinforcement strains of RC beams strengthened in shear with FRCM composites." *Proc., 8th*
619 *Biennial Conf. Adv. Comp. Constr. (ACIC 2017),* Sheffield, UK.
620 Gonzalez-Libreros, J. H., Sabau, C., Sneed, L. H., Pellegrino, C., and Sas, G. (2017). "State of Research
621 on Shear Strengthening of RC Beams Using FRCM Composites." Constr. Build. Mater., 149, 444-458.
622 Gonzalez-Libreros, J. H., Sneed, L. H., D'Antino, T., and Pellegrino, C. (2017). Behavior of RC beams
623 strengthened in shear with FRP and FRCM composites. Eng. Struct., 150, 830–42.
624 Grande, E., Imbimbo, M., and Rasulo, A. (2009). "Effect of transverse steel on the response of RC
625 beams strengthened in shear by FRP: Experimental study." J. Compos. Constr., 10.1061/(ASCE)1090-
626 0268(2009)13%3A5(405), 405-414.
627 Hashemi, S., and Al-Mahaidi, R. (2012). "Experimental and finite element analysis of flexural behavior
628 of FRP-strengthened RC beams using cement-based adhesives." Constr. Build. Mater., 26, 268–273.

629 ICC-Evaluation Service (2013). "Acceptance criteria for masonry and concrete strengthening using
630 fiber-reinforced cementitious matrix (FRCM) composite systems." *AC434*, Whittier, CA.
631 Italian National Research Council (CNR). (2004). "Guide for the design and construction of externally
632 bonded FRP systems for strengthening existing structures." *CNR-DT 200/2004*, Rome, Italy.
633 Italian National Research Council (CNR). (2013). "Guide for the design and construction of externally
634 bonded FRP systems for strengthening existing structures." *CNR-DT 200 R1/2013*, Rome, Italy.
635 Khalifa, A., Gold, W. J., Nanni, A., and Abdel Aziz, M. I. (1998). "Contribution of externally bonded
636 FRP to shear capacity of RC flexural members." J Compos. Constr., 10.1061/(ASCE)1090-
637 0268(1998)2%3A4(195), 195-202.
638 Loreto, G., Babaeidarabad, S., Leardini, L., and Nanni, A. (2015). "RC beams shear-strengthened with
639 fabric-reinforced-cementitious-matrix (FRCM) composite." Int. J. Adv. Struct. Eng., 7(4), 341–52.
640 Monti, G., and Liotta, M. A. (2007). "Test and design equations for FRP-strengthening in shear."
641 Constr. Build. Mater., 21, 799-809.
642 Monti, G., Santinelli, F., and Liotta, M. A. (2004). "Mechanics of FRP shear strengthening of RC
643 beams." *Proc., ECCM 11*, Rhodes, Greece.
644 Napoli, A., Realfonzo, R. (2015). "Reinforced concrete beams strengthened with SRP/SRG systems:
645 experimental investigation." Constr. Build. Mater., 93, 654–77.
646 Ombres, L. (2015). "Structural performances of reinforced concrete beams strengthened in shear with
647 a cement based fiber composite material." Compos. Struct., 122, 316–29.
648 Pellegrino, C., and Modena, C. (2002). "Fiber reinforced polymer shear strengthening of reinforced
649 concrete beams with transverse steel reinforcement." J. Compos. Constr. 10.1061/(ASCE)1090-
650 0268(2002)6%3A2(104), 104-111.
651 Raoof, S.M., Koutas, L.N., Bournas, D.A. (2016). "Bond between textile-reinforced mortar (TRM) and
652 concrete substrates: Experimental investigation." Comp. Part B, 98, 350-61.

653 Santandrea, M., Daissè, G., Mazzotti, C., and Carloni, C. (2017). "An Investigation of the debonding
654 mechanism between FRCM composites and a masonry substrate." Key Eng. Mater., 747, 382-389.
655 Sas, G., Täljsten, B., Barros. J., Lima, J., and Carolin, A. (2009). "Are available models reliable for
656 predicting the FRP contribution to the shear resistance of RC beams?" J. Compos. Constr.,
657 10.1061/(ASCE)CC.1943-5614.0000045, 514–34.
658 Sneed, L. H., Carloni, C., Baietti, G., and Fraioli, G. (2017). "Confinement of clay masonry columns
659 with SRG." Key Eng. Mater., 747, 350-357.
660 Sneed, L. H., Verre, S., Carloni, C., and Ombres, L. (2016). "Flexural behavior of RC beams
661 strengthened with steel-FRCM composite." Eng. Struc., 127, 686–99.
662 Täljsten, B., and Blanksvärd, T. (2007). "Mineral-Based bonding of Carbon FRP to strengthen concrete
663 structures." J. Compos. Constr., 10.1061/(ASCE)1090-0268(2007)11:2(120), 120-8.
664 Tetta, Z., Triantafillou, T. C., and Bournas, D. A. (2018). "On the design of shear-strengthened RC
665 members through the use of textile reinforced mortar overlays." Comp. Part B, 147, 178-196.
666 Tetta, Z.C., Koutas, L. N., and Bournas, D. A. (2015). "Textile-reinforced mortar (TRM) versus fiber
667 reinforced polymers (FRP) in shear strengthening of concrete beams." Compos. Part B, 77, 338–48.
668 The Concrete Society. (2012). "Design guidance for strengthening concrete structures using fibre
669 composite materials." TR 55, Crowthorne, UK.
670 Thermou, G. E., Katakalos, K., and Manos, G. (2015). "Concrete confinement with steel-reinforced
671 grout jackets." Mater. Struct., 48(5), 1355–76.
672 Triantafillou, T. C. (1998). "Shear strengthening of reinforced concrete beams using epoxy-bonded FRP
673 composites." ACI Struct. J., 95(2), 107-115.
674 Tzoura, E., and Triantafillou, T. C. (2016). "Shear strengthening of reinforced concrete T-beams under
675 cyclic loading with TRM or FRP jackets." Mater. Struct., 49(1), 17–28.

Figure captions

Fig. 1. (a) Tensile force in the composite material crossing the main diagonal crack. (b) Load response associated with a certain composite bonded length ℓ. (c) Peak load – composite bonded length relation, named capacity response in this paper.

Fig. 2. Scheme for the evaluation of the stress in the fibers.

Fig. 3. a) Matrix-fiber debonding interface. b) Cohesive debonding interface within the substrate. c) Cohesive material law (i) and (ii). d) Idealized load (stress) responses for FRCM composites with different bonded lengths with and without friction. e) Capacity responses for FRCM composites with and without friction.

Fig. 4. a) Different CMLs calibrated for PBO FRCM-concrete joints (Focacci et al. 2017). b) Comparison between analytical σ^*-ℓ curves and experimental results.

Fig. 5. Stress distribution in EB FRCM strips along the main diagonal shear crack.

688 **Table 1**. Parameters of the calibrated CMLs

CML	τ_m [MPa]	s_m [mm]	τ_f [MPa]	s_f [mm]	G_F [N/mm]
0_CML_-sp	0.39	0.17	0.03	1.57	0.24
1_CML-PL-τ3	0.30	0.01	0.03	1.11	0.18
2_CML-PL	0.29	0.19	0.01	3.21	0.24
3_CML-PL-τ3	0.28	0.22	0.03	$\rightarrow\infty$	-

689

690 **Table 2.** Mechanical properties of the PBO FRCM constituents

	f_{cm} [MPa]	σ_f [MPa]	E_f [GPa]
Matrix	28.4	3.5*	-
PBO fiber	-	3014	206

691 f_{cm}=average cylindrical compressive strength; σ_f=tensile strength; *determined by splitting tensile tests.

Table 3. RC beams strengthened in shear with U-wrapped PBO FRCM

Ref	Name	Geometry				Concrete and Steel				PBO FRCM						Results	
		b_w [mm]	d [mm]	h_w [mm]	a/d	f_{cm} [MPa]	A_s [mm^2]	A_{sw} [mm^2]	s_s [mm]	E_f [GPa]	σ_t [MPa]	i_f [mm]	w_f [mm]	β [°]	t_f [mm]	$V_{f,exp}$ [kN]	θ [°]
Ombres 2015	TRA2	150	225	250	3.00	30.8	628	101	292	206	3014	260	150	90	0.046	9.85	42.5
	TRB1	150	225	250	2.78	45.0	942	101	210	206	3014	1	1	90	0.046	33.83	34.0
Escrig et al. 2015	V-PMX750-01	300	254	300	2.76	34.1	603	101	500	206	3014	1	1	90	0.046	25.36	42.0
	V-PMX750-02	300	254	300	2.76	34.1	603	101	500	206	3014	1	1	90	0.046	32.70	40.0
Gonzalez-Libreros et al. 2017	S1-FRCM-F3-UN	150	250	300	3.00	23.3	2124	101	300	240	2500†	1	1	90	0.047	27.2	25.0
	S2-FRCM-F3-UN	150	250	300	3.00	24.7	2124	101	200	240	2500†	1	1	90	0.047	24.3	23.0

Note: b_w=beam web width; d=beam effective depth; h_w=beam web height; a=shear span; f_{cm}=average cylindrical compressive strength of concrete; A_s=area of tensile longitudinal steel reinforcement; A_{sw}=area of transverse steel reinforcement; s_s=center-to-center transverse steel reinforcement spacing; E_f=fiber elastic modulus; σ_t=fiber tensile strength; i_f=center-to-center FRCM strip spacing measured along the beam longitudinal axis; w_f=width of the FRCM strip perpendicular to the fiber direction; β= angle of the longitudinal fibers with respect to the beam longitudinal axis; t_f=equivalent fiber thickness; $V_{f,exp}$=shear strength contribution provided by the FRCM; θ=angle of main shear crack angle with respect to the beam longitudinal axis; †Provided by the manufacturer.

Table 4. Results and assessment of the shear strength analytical model

Ref	Name	Results			Analytical model								Assessment				
		$V_{f,exp}$ [kN]	θ [°]	$\Delta\xi_{cr}$ [mm]	$\Delta\xi_a$ [mm]	ξ_{max} [mm]	$\sigma_{fe,e}$ [MPa]	$\sigma_{fe,3}$ [MPa]	$\sigma_{fe,2}$ [MPa]	$V_{f,e}$ [kN]	$V_{f,3}$ [kN]	$V_{f,2}$ [kN]	$r_{exp,e}$ [%]	$r_{exp,3}$ [%]	$r_{exp,2}$ [%]	$r_{e,2}$ [%]	$r_{3,2}$ [%]
Ombres 2015	TRA2	9.85	42.5	300	385	1640	1212	1207	1100	14.22	14.15	12.91	-30.7	-30.4	-23.7	10.2	9.7
	TRB1	33.83	34.0	362	465	1981	1212	1207	1100	33.48	33.33	30.39	1.1	1.5	11.3	10.2	9.7
Escrig et al. 2015	V-PMX750-01	25.36	42.0	342	389	1656	1281	1279	1186	29.92	29.88	27.70	-15.2	-15.1	-8.4	8.0	7.9
	V-PMX750-02	32.70	40.0	356	404	1724	1281	1279	1186	32.10	32.07	29.72	1.9	2.0	10.0	8.0	7.9
Gonzalez -Libreros et al. 2017	S1-FRCM-F3-UN	27.2	25.0	532	615	7373	619	662	607	28.07	30.04	27.55	-3.1	-9.4	-1.3	1.9	9.0
	S2-FRCM-F3-UN	24.3	23.0	576	665	7975	619	662	607	30.83	33.00	30.26	-21.2	-26.4	-19.7	1.9	9.0

Figure_1

Click here to access/download;Figure;Fig_1.tiff

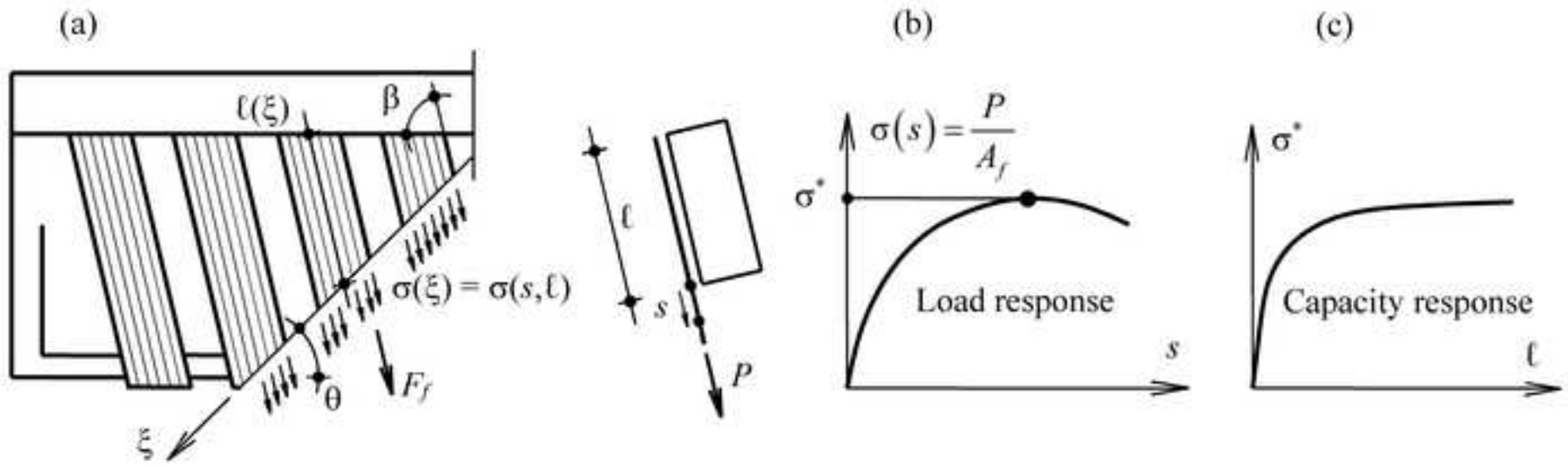

Figure_2

Click here to access/download;Figure;Fig_2.tiff

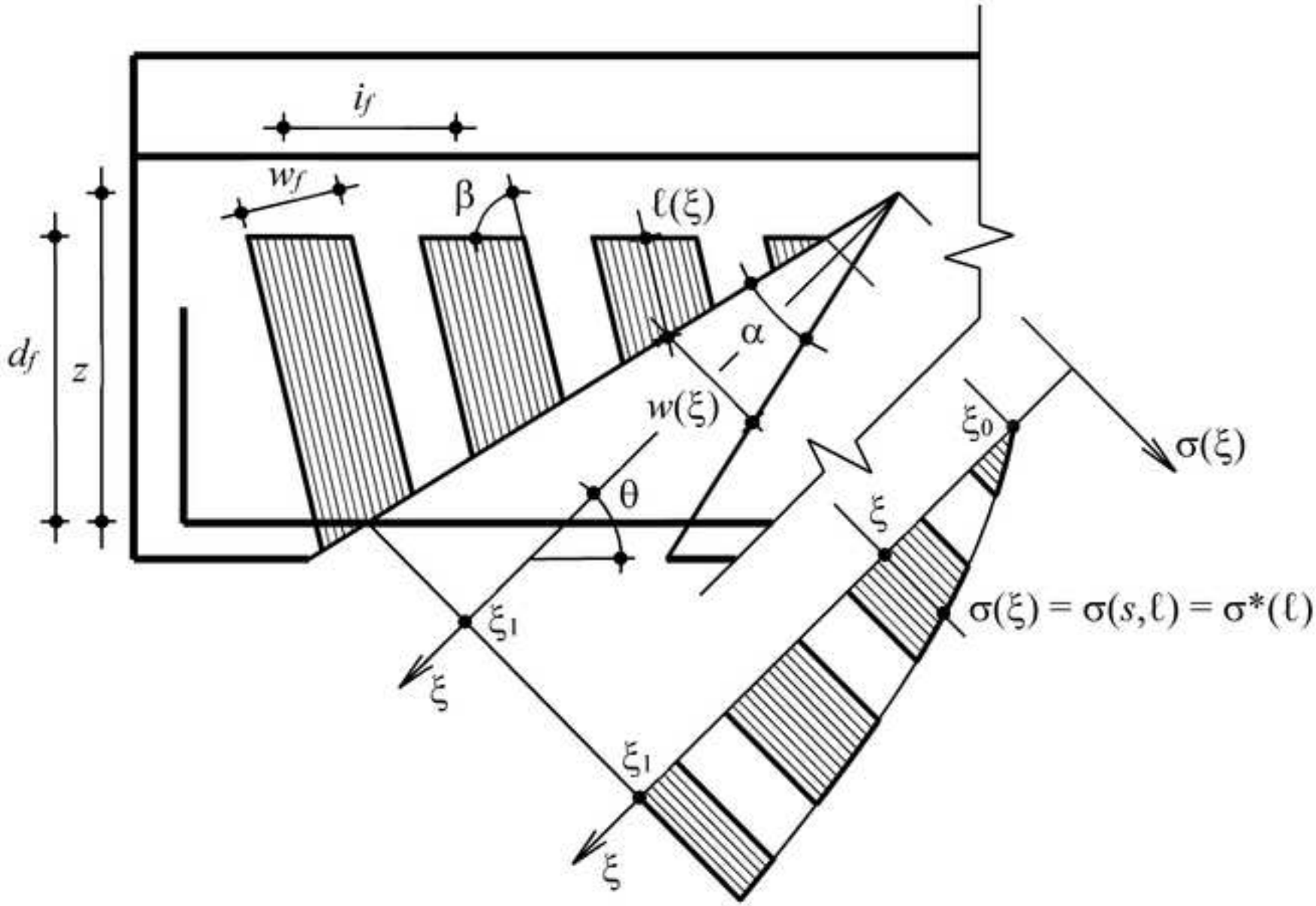

Figure_3

Click here to access/download;Figure;Figure 3.tiff

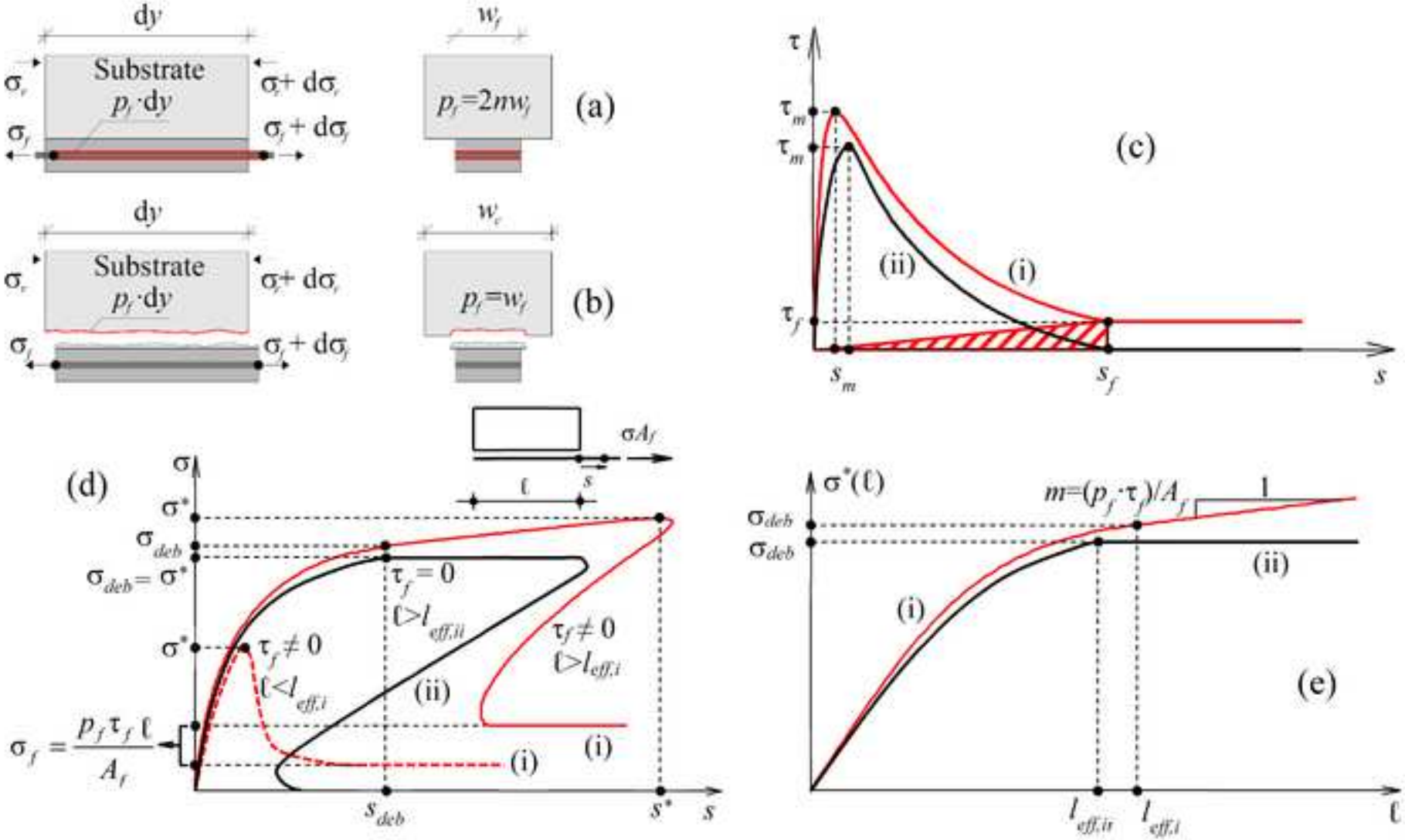

Figure_4a

Click here to access/download;Figure;Figure_4a.tif

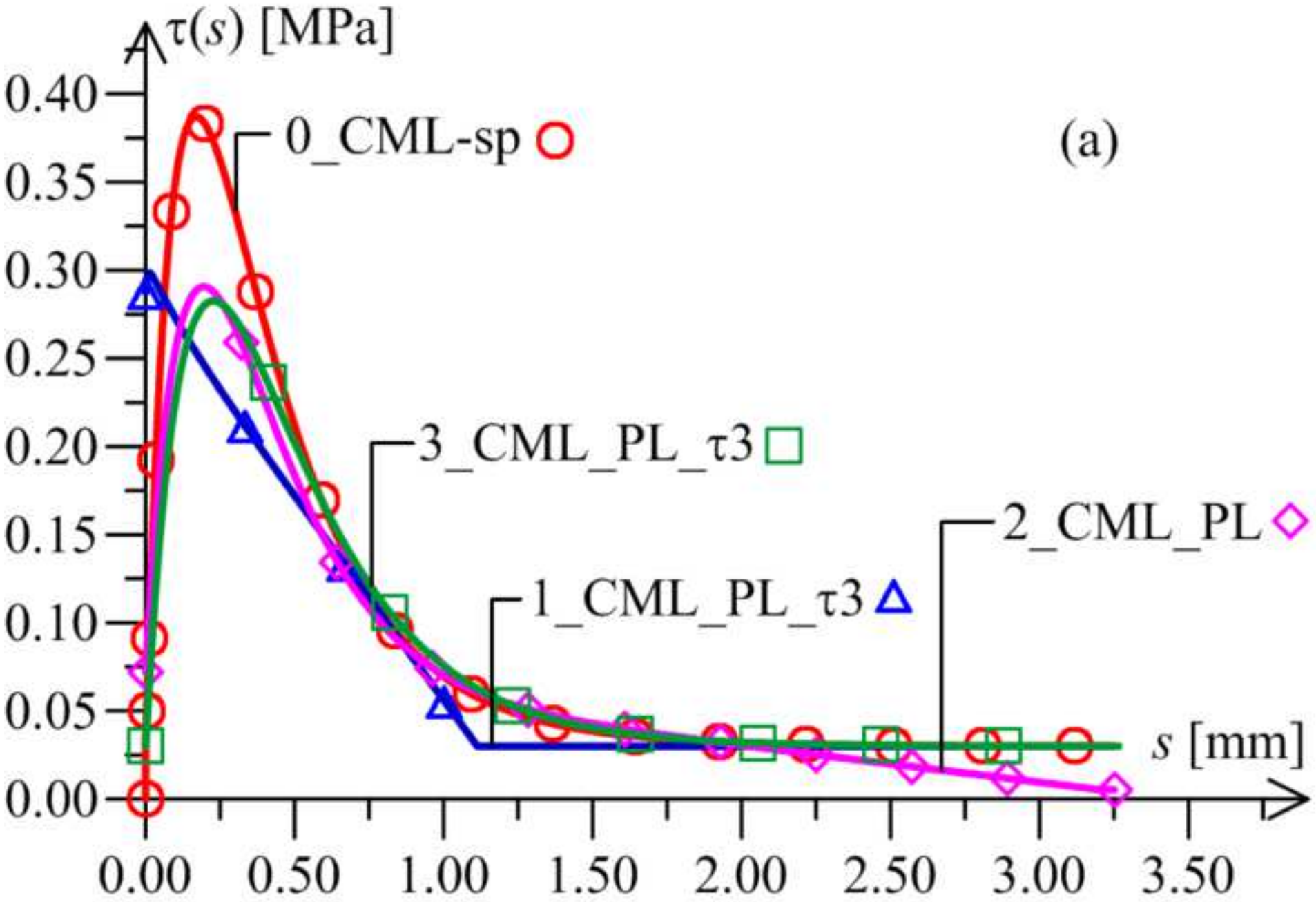

Figure_4b

Click here to access/download;Figure;Figure_4b.tif

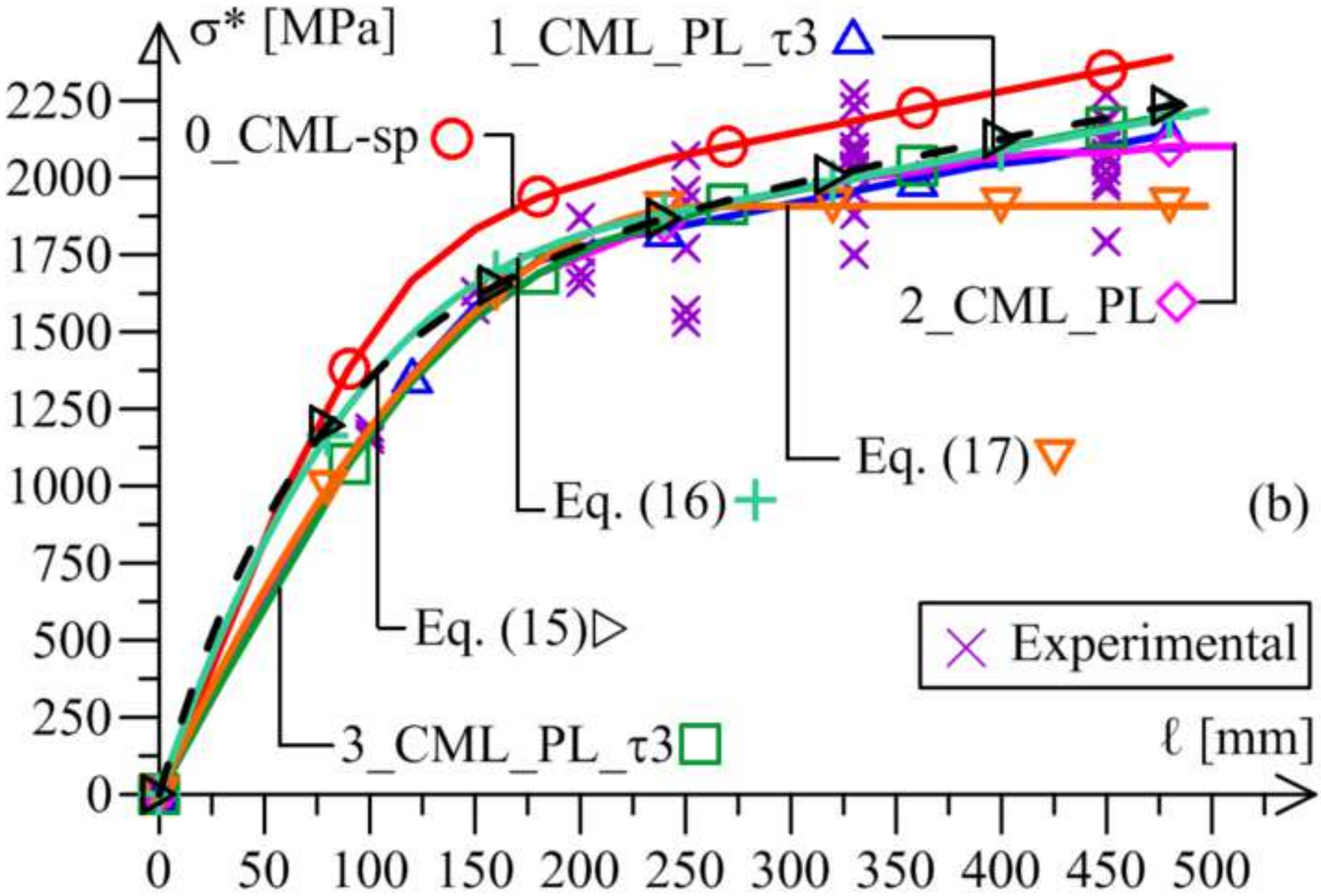

Figure_5

Click here to access/download;Figure;Fig_5.tiff